

# Visual encoding: Principles and software

# 11

Brian A. Wandell<sup>a,\*\*</sup>, David H. Brainard<sup>b</sup>, and Nicolas P. Cottaris<sup>b</sup>

<sup>a</sup>*Psychology Department and the Stanford Center for Image Systems Engineering, Stanford University, Stanford, CA, United States*

<sup>b</sup>*Department of Psychology, University of Pennsylvania, Philadelphia, PA, United States*

\*Corresponding author: e-mail address: wandell@stanford.edu

---

## Abstract

For more than two centuries scientists and engineers have worked to understand and model how the eye encodes electromagnetic radiation (light). We now understand the principles of how light is transmitted through the optics of the eye and encoded by retinal photoreceptors and light-sensitive neurons. In recent years, new instrumentation has enabled scientists to measure the specific parameters of the optics and photoreceptor encoding. We implemented the principles and parameter estimates that characterize the human eye in an open-source software toolbox. This chapter describes the principles behind these tools and illustrates how to use them to compute the initial visual encoding.

---

## Keywords

Display, Radiance, Irradiance, Computer graphics, Optics, Lens, Point spread function, Pigment density, Photoreceptor, Cone fundamentals, Cone mosaic, ipRGC, Retina

---

## 1 Introduction

There are many reasons why a scientist or engineer may want to calculate the initial encoding of light by the eye. First, the encoding by the photoreceptors impacts all of visual perception, including how we perceive shape, pattern, motion, and color. For example, the retina encodes some information and is blind to other information. The initial encoding is important to vision scientists because it impacts many subsequent visual judgments.

Second, display designers who create images to be viewed by the eye, and camera designers who are interested in estimating which aspects of the scene the viewer sees, can benefit from calculating how light will be encoded by the eye. Knowing the limits of human visual encoding is essential for specifying display and camera requirements.

Third, cortical and thalamic neuronal responses depend on their inputs as well as their intrinsic circuitry. Signals initiated in the retina are a major part of what drives responses in thalamus and cortex. To model understand these responses, neuroscientists studying the visual pathways benefit from quantifying the visual inputs.

For these and other reasons, scientists and engineers have worked over several centuries to establish the principles and measure the parameters of the initial visual encoding (Wandell and Brainard, 2022); many principles and parameters have been reported in the literature. We used this information to create a computational tool to estimate the photopigment excitation rate of the cones in a typical human photoreceptor mosaic. Over time, we will extend this toolbox to model other neuronal responses. The open-source Matlab toolbox (Image Systems Engineering Toolbox for Biology, ISETBio) (Wandell et al., 2022) includes computational methods and data that model the visual encoding. Here we describe how the underlying ideas are implemented. We also provide examples that use the ISETBio code in a repository that accompanies this chapter.<sup>a</sup>

A simulation of the visual encoding begins with a description of the visual scene. This is used to compute the image formed by the physiological optics at the retina. Many different types of scenes may be of interest, ranging from stimuli presented on traditional flat emissive displays to complex three-dimensional scenes with multiple objects and lights. The software needed to simulate the retinal image from these different types of scenes varies considerably in complexity. To make the ISETBio computations more useful, we provide tools that compute the retinal image from a description of the radiance for two-dimensional (planar) scenes (e.g., traditional displays or three-dimensional scenes viewed at a large distance), and we also provide methods that enable scientists and engineers to work with descriptions of realistic three-dimensional spectral scenes (ISET3d) using quantitative computer graphics (Physically Based Ray Tracing, PBRT) (Pharr et al., 2016). With the latter methods the user can define a three-dimensional scene and generate the spectral irradiance of the incident light field arriving at the cornea and the spectral irradiance image formed on the retina (Lian et al., 2019). The ability to work with complex three-dimensional scene descriptions broadens the set of ideas that can be explored in simulation.

---

## 2 Representing the scene radiance

We first present methods that are useful for two-dimensional (planar) scenes. As noted above, these are applicable to traditional flat displays and to three-dimensional scenes viewed at a large distance. We then describe tools for calculating the incident light field and retinal image from a three-dimensional scene specification.

---

<sup>a</sup><https://github.com/isetbio/isetbioencoding/wiki>

## 2.1 Planar scenes: Calibrated display

Vision science laboratories often experiment using stimuli presented on flat display. A wide range of display technologies have been used: cathode-ray tubes (CRTs), liquid-crystal displays (LCDs), and organic light-emission diode (OLED) displays. From the point of view of the vision scientist or imaging engineer, all of these display technologies emit a radiance from a large number of discrete regions (pixels) on the display surface (Fig. 1). In addition to their use in the lab, such displays are used widely by consumers. Indeed, you may well be reading this chapter on such a display.

The radiance emitted from each display region (pixel),  $E(x, y, \lambda)$ , is the weighted sum of three primaries (subpixels) with spectral distributions  $R(\lambda)$ ,  $G(\lambda)$ , and  $B(\lambda)$ . The values in an image file specify the intensities of the three primaries at each point  $(r(x, y), g(x, y), b(x, y))$ .<sup>b</sup> We neglect directional dependency in our formulation here

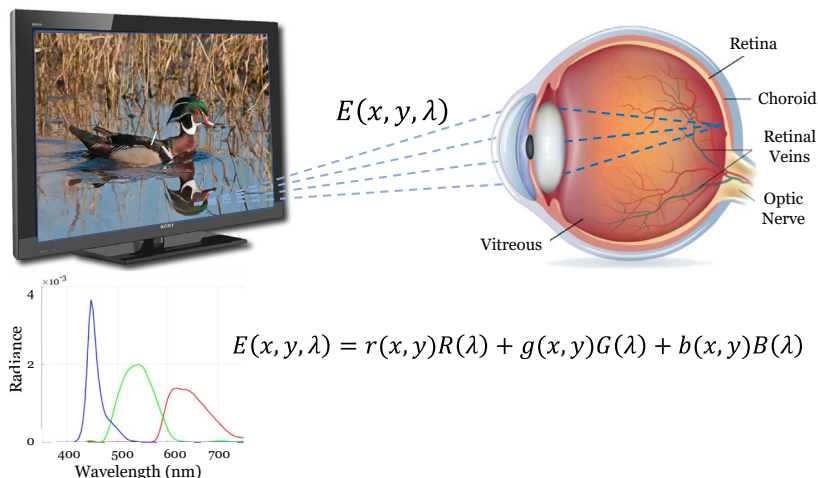


**FIG. 1**

Display radiance. A display emits a spectral radiance from each small spatial region  $r(x, y)$ . Within each region (pixel) the display radiance is the weighted sum of the emissions of the display primaries (plus potentially some amount of reflected ambient light, not shown). The radiance from each region is the weighted sum of the primaries, and the weights depend on the image. The rays are emitted in many directions, and only a small fraction of the ray bundle reaches the cornea, forming the incident light field. The physiological optics (cornea and lens) transform the light at the cornea into the retinal irradiance. The lens of the eye accommodates to focus the relevant portion of the image at the cone inner segment layer of the retina.

<sup>b</sup>There is typically a nonlinear relationship that maps the digital values represented in an image file (*RGB*) to the relative intensities of the display primaries (*rgb*). We account for this nonlinearity, often called the “gamma function” in our display models and simulations, but for clarity we do not dwell on this static nonlinearity in this chapter.

because, generally, vendors try to make display emission stable over a wide range of angles. For applications where precise simulation of viewing direction is important, the primaries may be calibrated from the same direction as the display will be viewed.

The ISETBio function “sceneFromFile” calculates the spectral radiance from a calibrated display, accounting for the display properties (e.g., pixel sampling density, spectral radiance of the primaries, and the nonlinear function relating the digital values to the intensities of the display primaries).

```
filename = fullfile(isetRootPath,'data','images','rgb','woodDuck.png');
meanLuminance = 50;
scene = sceneFromFile(filename,'RGB',meanLuminance,'LCD-Apple');
sceneWindow(scene);
```

In this code example, filename is a string specifying the image file location on the host computer system. The ISETBio repository includes calibrated description of several different displays; here a description of an LCD display is used. The code example here also adjusts the mean luminance of the spectral radiance image to be  $50 \text{ cd/m}^2$ . Additional information on display calibration and conversion of digital values to spectral radiance may be found in [Brainard et al. \(2002\)](#).

## 2.2 Planar scenes: Natural image approximation

Satisfactory visual displays are built with only three primaries because the retina contains three types of cone photoreceptors. The relative intensity of the three primaries controls the relative excitation of the three types of cones. The understanding that arbitrary spectra can be matched with a mixture of three primaries was developed by Thomas Young, James Clerk Maxwell, Hermann von Helmholtz, and many others. The principles underlying matching and their use in modern vision science, and particularly the concept of the color-matching experiment and metamerism ([Maxwell, 1860](#)), are described in numerous sources (e.g., [Brainard and Stockman, 2010](#); [Wandell, 1995](#); [Wandell and Brainard, 2022](#)).

The spectral radiances created by the weighted sum of typical display primaries (LCD, OLED, and CRT) are unlike those in nature. For many simulation applications, however, we would like to use the image file to simulate a scene with a plausible natural spectral radiance. We do this in ISETBio by creating a theoretical display with three primary spectra whose linear combinations better approximate the space of naturally-occurring spectral radiance distributions. This theoretical display is included in ISETBio ([Fig. 2](#)). The display primaries span the subspace defined by the first three principal components of natural surface reflectances,  $S_i(\lambda)$ ,

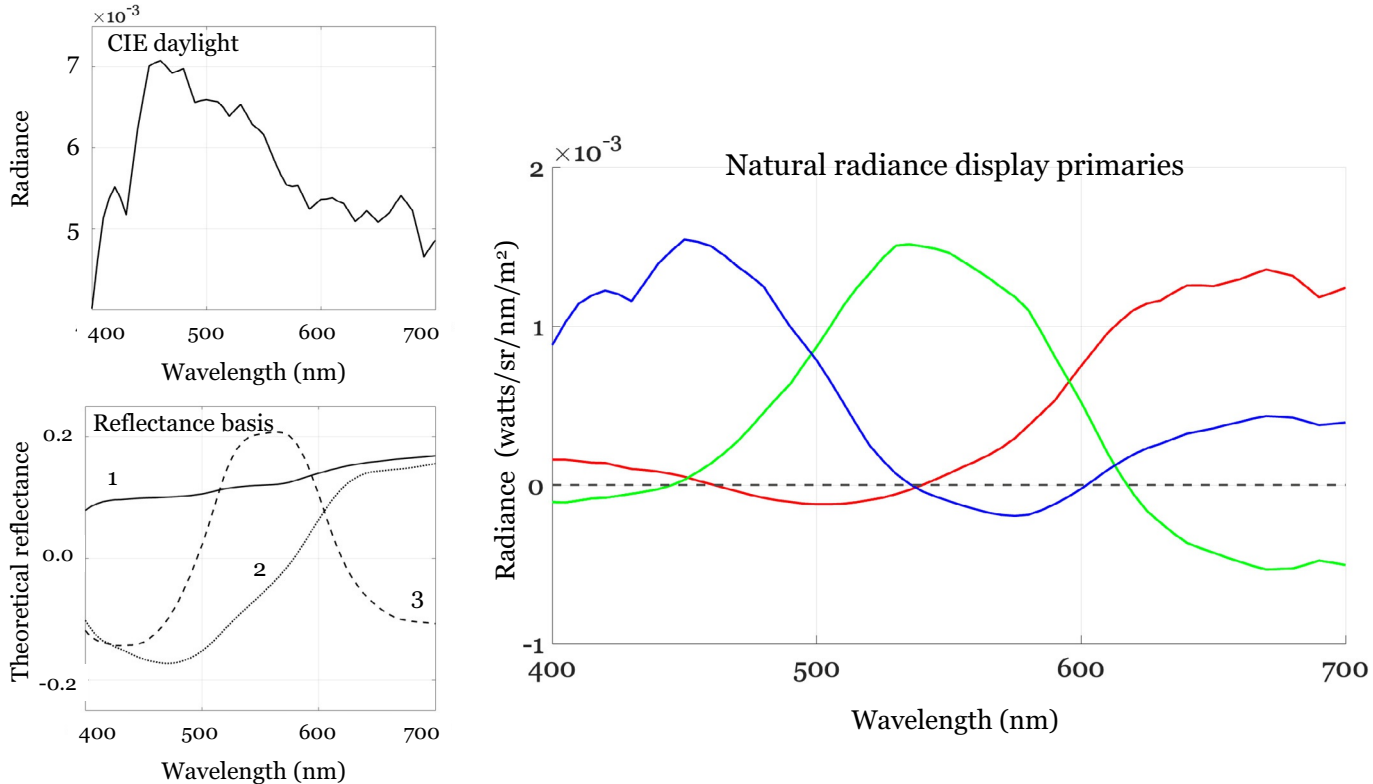


**FIG. 2**

The natural radiance display. For most displays the emitted spectral radiance is unlike the spectral radiance observed in nature. It can be useful to convert an RGB image into a scene spectral radiance that matches the appearance for a standard display (sRGB) but that also has a natural spectral radiance. ISETBio includes a method, based on a theoretical display, that accomplishes this. See text for details.

illuminated by a D65 daylight spectral radiance  $D_{65}(\lambda)$ . The three functions,  $B_i(\lambda) = S_i(\lambda)$ ,  $\circ D_{65}(\lambda)$  provide a linear basis that approximates natural scene spectra.

We discretize these basis functions over a set of sample wavelengths and combine them into the columns of a matrix  $B$ . Many weighted sums of these columns will produce a plausible natural scene radiance (subject to a nonnegativity constraint). To render a specific image, however, we must find a method to map  $rgb$  values in the image into the primary intensities for the theoretical display. Let  $r_{3 \times 1}$  be a vector containing the  $rgb$  values at a display location, and similarly let  $p_{3 \times 1}$  be a vector with the intensities for the theoretical display. We find a transformation matrix  $T_{3 \times 3}$  so that the  $p = Tr$  values presented on the theoretical display produce the same CIE XYZ tristimulus values as the values  $r$  presented on a standard, sRGB, display (IEC, 1999).<sup>c</sup> To meet this criterion we create a matrix  $C$  with columns containing the CIE standard color matching functions  $\bar{x}(\lambda), \bar{y}(\lambda), \bar{z}(\lambda)$ , and we create a matrix  $S_{3 \times 3}$  that maps the linear primary values  $rgb$  to the CIE XYZ values for an industry-standard sRGB display. Then  $T$  must satisfy

$$Sr = C'BT r \quad (1)$$

for any choice of  $r$ . It follows that

$$T = (C'B)^{-1}S \quad (2)$$

and thus the primary intensities on the theoretical display must be  $p = Tr$ .<sup>d</sup>

Finally, we can express the primaries of the theoretical display as the columns of  $BT$  (Fig. 2). This theoretical display will then directly render the image  $rgb$  values as spectral radiances that approximate naturally occurring spectra.

### 2.3 Display variation

A reasonable conclusion to draw from the discussion above is that an image file presented directly on different display models can produce substantially different spectral radiance images. We compare the images from a calibrated LCD, a calibrated OLED, and the theoretical display in Fig. 3. The LCD and OLED display primaries differ from one another in both their peak wavelengths and bandwidths. The CIE XYZ values of the image data rendered on these two displays differs because the display primaries differ. These differences are substantial for quantitative simulations.

The spectral radiance distribution from the theoretical display is created to match natural spectral radiance data under a  $D_{65}$  illuminant, and for this reason it differs substantially from the radiance emitted by the real displays. The CIE XYZ tristimulus values from the theoretical display are designed to match those of an industry standard, but theoretical, sRGB display. The image appearance on the real displays

---

<sup>c</sup>The XYZ tristimulus values capture the results of human color-matching experiments such that two spectra that have the same tristimulus values match in appearance to a human observer (Brainard and Stockman, 2010; Wandell, 1995).

<sup>d</sup>Wandell (1995) and Brainard and Stockman (2010) develop the matrix-vector approach to this sort of calculation in more detail.

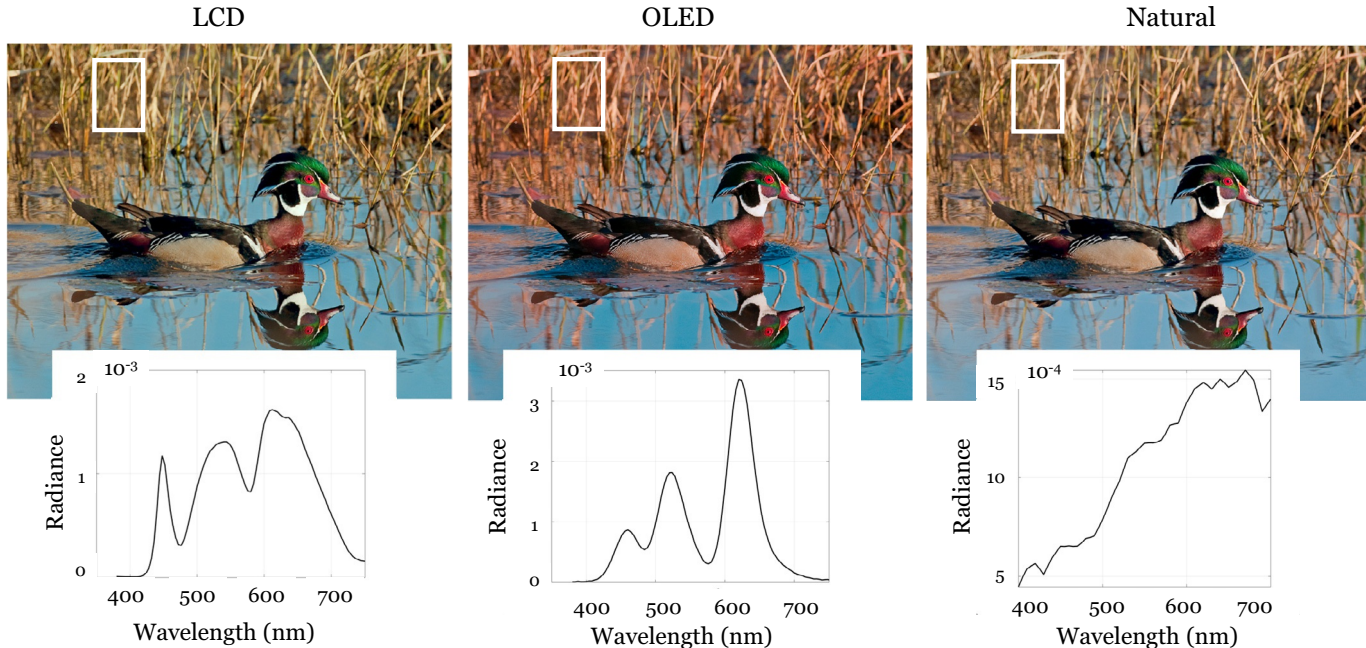


**FIG. 3**

RGB image data to radiance-display model. ISETBio converts RGB data from an image file into a spectral scene representation by assuming the image will be shown on a calibrated display. The three images render the same RGB data on different calibrated displays. The mean spectral radiance from a small region (*white rectangle*) is shown for each display. The *left* is an LCD, the *center* an OLED display and the *right* a theoretical display designed to produce scene radiance similar to natural radiances under a D65 illuminant. The images in this figure were produced by transforming the simulated spectral radiances of the several displays into CIE XYZ values. We then created sRGB image files corresponding to each displayed image for use in the figure. The image appearance differences illustrate that simply copying RGB values into the frame buffer generates substantial color appearance differences across the displays. Differences of this magnitude are typical of the variation observed when displaying RGB data without correcting for the display primaries and other factors.

differ from one another and the sRGB standard. In our experience, such variations are typical of actual displays. The variations across displays can be eliminated by using image rendering procedures that take display calibration measurements into account; we do not illustrate these procedures here.

To summarize, ISETBio methods transform the RGB data in an image file into planar spectral radiance scenes for simulation. The transformation enables the user to simulate the spectral radiance in an experimental setup for a calibrated display; or, by using the theoretical display to simulate a spectral radiance that is similar to what one might observe in a natural scene. The choice of displays, or simulated reflectance basis and illuminant, provide the user with considerable flexibility. For engineering applications, re-running simulations across a range of displays provides an approach to checking the robustness of conclusions with respect to display variation.

## 2.4 Three-dimensional scenes

Quantitative computer graphics simulations can significantly expand the range of phenomena explored by vision scientists. Ray tracing methods provide accurate estimates of the scene radiance, and they enable labeling the pixels of the rendered image with the values of the underlying scene parameters (e.g., reflectance, surface normal). Furthermore, computer graphics provides the user with a significant degree of control over the properties of the scene, including material and lighting spectral properties, transparency, and surface inter-reflections. Many of these properties impact visual judgments, but are either difficult or impossible to control in experimental rigs; simulation is our best current approach to analyze how these scene properties impact perception. Simulating three-dimensional scenes with user-specified lighting and material properties, and then calculating the expected cone excitations and neural responses from these scenes, may provide useful information to model and understand visual appearance judgments (Fleming, 2017; Heasly et al., 2014).

Renderings of several three-dimensional scene radiance distributions that illustrate the ability to change camera position and material properties are shown in Fig. 4. The images show a moderately complex scene (150 objects) that contain multiple materials (wood, marble, glass, metal). The scene is rendered using complex global illumination (light from a window) from different eye positions.

The computer graphics simulation generates scene radiance descriptions that we rendered into RGB images for display in the figure. The underlying scene radiance data are quantitative, and certain aspects—such as the spectra and the large dynamic range—cannot be represented accurately in RGB images at typical quantization levels. For example, the dynamic range of the radiance from the images with the highly specular metal pieces can be four orders of magnitude. Such high-dynamic ranges can arise in natural images and must be managed by the retinal encoding. How the visual system quickly comes to distinguish and

**FIG. 4**

Renderings (RGB) of simulated three-dimensional scene spectral radiance distributions. The scene is constructed using more than 150 different objects and a dozen different materials. The *top* renderings show the scene from the same point of view and lighting, but with different material properties assigned to the objects (glass, mirror, marble, mahogany). The *bottom* renderings change the camera point of view with respect to the global lighting, but maintain the same materials. The object identities remain recognizable as the views and materials change, and aspects of the global illumination (not shown) can be inferred from the highlights (gloss). Studying visual perception of natural scenes is likely to require the ability to create and control such images.

identify the glass and metal chess pieces is an interesting question that is the topic of considerable recent research (see [Fleming \(2017\)](#) for a review).

Many topics in vision science can benefit from having quantitative information about three-dimensional scenes. Stereo vision, depth generally, vergence, accommodation, and parallax require a specification of the distance from the eyes to objects in the scene. Finally, we note that knowledge of how lighting and materials impact the retinal image may be helpful when designing light sources in complex indoor environments ([Pont, 2019](#)). These simulations may also be helpful in understanding how lighting impacts circadian rhythms through the intrinsically photosensitive retinal ganglion cells (ipRGCs) ([Zandi et al., 2021](#)).

Computational methods for rendering three-dimensional scenes are implemented in ray tracing tools, such as PBRT (Pharr et al., 2016) and Mitsuba (Nimier-David et al., 2019). The ISET3d toolbox, which is tightly integrated with ISETBio, provides an interface to the open-source and carefully documented PBRT software (Pharr et al., 2016). Further, we added methods to PBRT that simulate fluorescence, spectral textures, and optics (Goossens et al., 2022; Lian et al., 2019; Lyu et al., 2021). A main purpose of the ISET3d toolbox is to provide a programming interface that helps users create natural scenes and control lighting, material properties, and scene geometry, and that interoperates with the ISETBio and ISETCam (Wandell, 2022) toolboxes.<sup>e</sup>

---

### 3 Optics: The retinal irradiance

If the scene radiance originates from a plane (e.g., a flat display), the optical transformation from radiance to retinal irradiance can be approximated by a linear calculation that sums the rays arriving at the retina from each point in the plane. The spatial distribution of the retinal irradiance arising from a point can be specified by knowing the position of the point and the wavelength of the light. This is called the point spread function (PSF).

For a three-dimensional scene the computation differs for three main reasons. First, for fixed accommodation of the eye, the PSF depends on the distance to the point. Second, some of the rays from a 3D point may be blocked by closer objects (occlusion). Third, rays emitted from a point may reach the retina after scattering off of other objects (inter-reflections). Thus, the retinal image from a point in three-dimensional space depends not only on the position of the point but also on the positions and material properties of other objects in the scene.

Because calculation requirements differ between planar and full 3D scenes, we created two types of physiological optics models. One calculation is well-suited for planar scenes, such as employed in typical psychophysical and biological experiments. This calculation is based on the PSF. The second calculation uses a human eye model that is integrated into ray-tracing software (PBRT). This calculation generates the retinal spectral irradiance from a three-dimensional scene, accounting for occlusions, inter-reflections, and material properties (Lian et al., 2019). The accuracy of the PBRT ray trace calculation has been experimentally tested and quantified (Lyu et al., 2021).

---

<sup>e</sup>Like many others we have experienced the complexity of downloading and installing large software packages and their dependencies. To simplify installation, we inserted the modified PBRT into a Docker container that can be invoked from within ISET3d. The code executes on machines that support containers, including Mac OS, Windows, and Linux.

### 3.1 Image formation: 2D

Because of the strong chromatic aberration of the eye, the human PSF depends on wavelength. The PSF also depends on the visual field position of the point. To calculate the retinal irradiance, we need to know the PSFs across wavelength and the visual field. The sum of the light blurred by the PSFs across all visual field points and for each wavelength yields the spectral irradiance distribution at the retina (retinal spectral irradiance, or retinal image). The PSFs also differ across individuals.

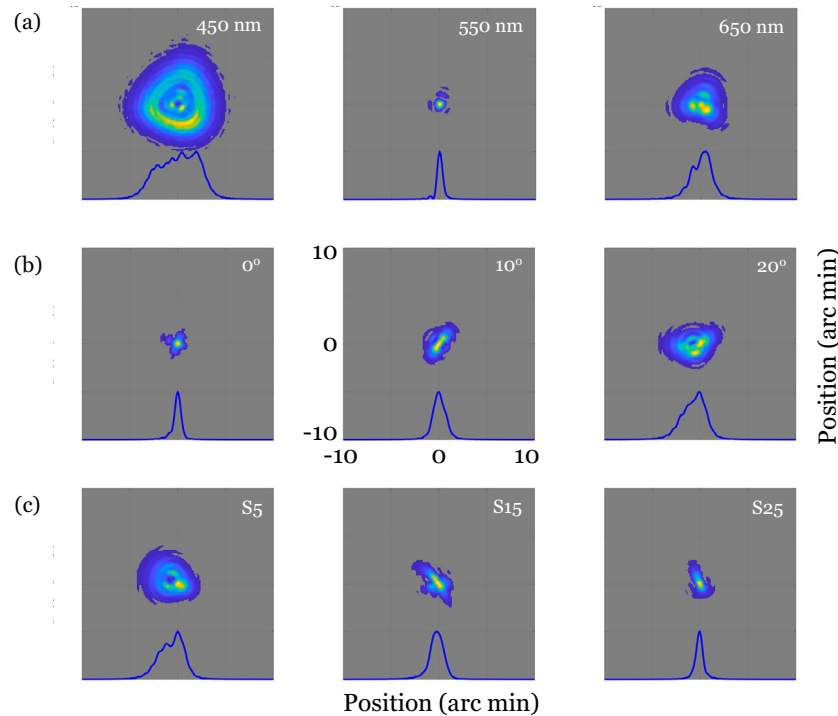
#### 3.1.1 Space- and wavelength-varying PSFs

Since the late 1990s, we have been able to measure the *in vivo* human PSF by using wavefront sensors (Liang et al., 1997). These instruments measure an image reflected from the retina. The reflected images are analyzed through an array of microlenses, enabling measurement of the angular deviation of the reflected rays across the pupil, relative to perfect focus. These angular deviations are used to compute the pupil function, a complex-valued function that specifies the relative optical phase of the light passing through each location of the pupil. The pupil function is related to the PSF through the modulus of its Fourier transform. The wavefront sensor measurements characterize the fine structure of the PSF at a much higher resolution than earlier methods.

The aberrations in the pupil function are commonly approximated as the weighted sum of Zernike polynomials—these are polynomials that are defined over a circular support. The Zernike polynomial coefficients provide an interpretation of the pupil function in terms of different physical effects. For example, one of the coefficients defines the effect of defocus, another astigmatism, and so on.

The pupil function, and thus the PSF, varies with several imaging parameters. The largest effect is the dependence on wavelength (Fig. 5a). This difference is relatively consistent across subjects because much of it is due to the index refraction of water in the eye (Wandell, 1995). As a first approximation, a measurement of the pupil function at one wavelength is sufficient to compute the entire polychromatic PSF. This extrapolation is done by adjusting the Zernike polynomial term for defocus as a function of wavelength. In addition, measurement of the pupil function for a dilated pupil allows calculation for smaller pupils simply by appropriately vignetting the function before taking its Fourier transform.

The measured PSF also depends on eccentricity (Fig. 5b) and between subjects (Fig. 5c), as the figure shows. But these differences are less consistent and often not as large. Several authors have shared measurements of the human pupil function (and thus the PSF) in typical subjects (Jaeken and Artal, 2012; Polans et al., 2015; Thibos et al., 1990). Curated versions of these data are included in ISETBio. The PSFs can be used to calculate the retinal irradiance and cone excitations from the planar image radiance, at specified visual field locations, wavelengths, and for different subjects.

**FIG. 5**

Physiological optics. The images represent the human point spread function (PSF), measured at different wavelengths and visual field positions. The blue lines are a one-dimensional profile obtained by summing the PSF down the columns. (a) Comparisons at different wavelengths for one subject in the fovea. (b) Comparison at different eccentricities for another subject at 550 nm. (c) Comparisons of three additional subjects at 550 nm and 5 degrees eccentricity. The PSFs and profiles were calculated using data from [Jaeken and Artal \(2012\)](#).

### 3.1.2 Shift-invariant PSFs

Over some portion of the visual field, image formation through the optics can be well-approximated as shift invariant; that is, the PSF remains approximately constant. This is a useful computational advantage because we can then compute the retinal spectral irradiance by convolving each wavelength of the scene spectral radiance with a wavelength-dependent PSF ([Wandell and Brainard, 2022](#)).

ISETBio implements these computations using a data structure that represents the radiance of the displayed image (“scene”), and a separate data structure that represents the optical information arriving at the retina (“oi”, short for “optical image”).

Above we illustrated how to create an ISETBio scene from an RGB image file and a description of a calibrated display. The retinal irradiance from the scene is calculated over a shift-invariant region like this:

```
% The default OI is a model of the human foveal optics  
oi = oiCreate;  
  
% Convert the scene spectral radiance to retinal spectral  
irradiance  
oi = oiCompute(oi,scene);  
  
% View a rendering of the spectral irradiance image  
oiWindow(oi);
```

The optics parameters that influence the PSF (e.g., pupil size, example subject, wave-front aberrations) can be read or set using the `oiGet` and `oiSet` functions. For example, to create an `oi` structure that represents measurements of a subject from one of the databases, we use the following ISETBio function with explicit key/value pairs:

```
oi = oiPosition('Artal2012', ...  
    'position',[5,0], ...  
    'eye side','right', ...  
    'subject rank',5);
```

A practical question is this: How large is the shift-invariant region? Using a strict criterion based on the wavefront aberration size, the region has been estimated to be less than  $\pm 0.5$  degree (Bedggood et al., 2008). An alternative criterion, which is more practical, assesses the shift-invariant region with respect to the cone excitations. We calculate whether the two different point spread functions predict significantly different cone excitations. To determine significance, we might measure the difference divided by the standard deviation of the Poisson variability in excitations. An assessment at the level of the cones is appropriate for the goals of many ISETBio calculations.

An example of such a comparison is illustrated in Fig. 6. We calculate the edge spread function (how light spreads from a light to dark edge) in the cone mosaic, and we compare the spread with respect using a synthesized cone mosaic centered at 1 degree eccentricity. Scripts in the GitHub repository for this chapter illustrate how to

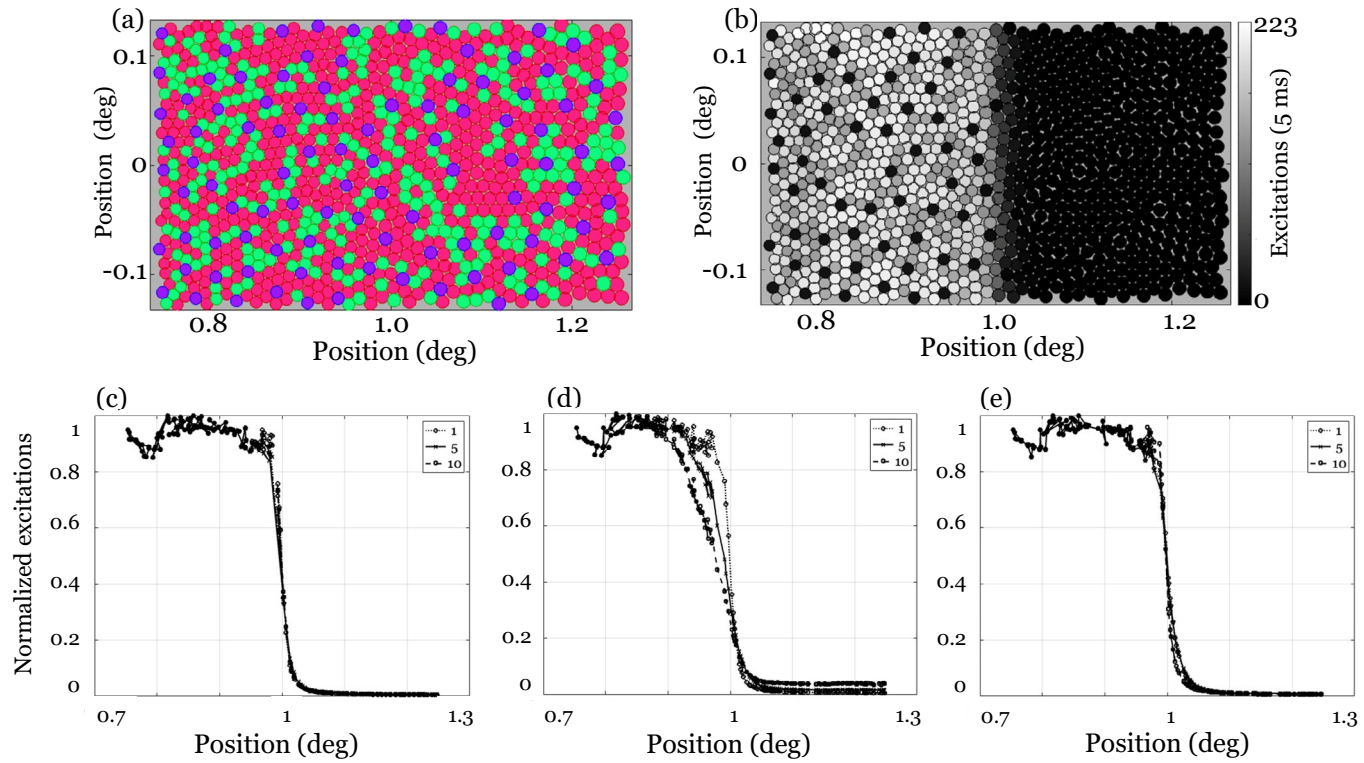


**FIG. 6**

Optical shift-invariance. We can assess the importance of the optical blur by calculating its impact on the responses in a cone mosaic. In this example, we compare the edge-spread function (ESF) of an edge at three different eccentricities. (a) First we synthesize a typical cone mosaic near 1 degree eccentricity. (b) Then, we compute the number of excitations in each cone in response to a sharp edge (broad spectrum, 5 ms exposure). (c–e) Using wavefront measurements from three different subjects, we compute the L-cone excitations in this mosaic. Each panel is for a different subject. Within each panel we compare the ESF using wavefront data measured at 1, 5, and 10 degrees. For two subjects (c, e), the ESF is the same at these eccentricities. For one subject (D) the edge spread changes with eccentricity. Wavefront data from ISETBio subjects 15, 49, and 51, measured by [Jaeken and Artal \(2012\)](#). The ISETBio script for this figure makes this comparison for many other subjects and stimuli.

perform this analysis using different stimuli and subjects. Our experiments suggest that convolution is a reasonable approximation for many subjects over the central 10 degrees. Of course, more could be done to test this proposition. Note that we explain the computation of cone excitations in more detail below; here we only compute the mean excitations of each cones and do not take the illustrative calculation through to a statistical evaluation of the differences in excitations.

### 3.1.3 Diffraction

An optical system with ideal spatial resolution is said to be diffraction limited. For a circular pupil the PSF of a diffraction-limited system will be the Airy disk pattern. The diameter ( $d$ ) of the Airy disk (first zero crossing) will depend on the f-number ( $F$ , ratio of focal length to aperture diameter) and the wavelength ( $\lambda$ ) of the light,

$$d = 2.44F\lambda. \quad (3)$$

ISETBio creates a diffraction-limited 'oi' and sets the f-number of the optics this way:

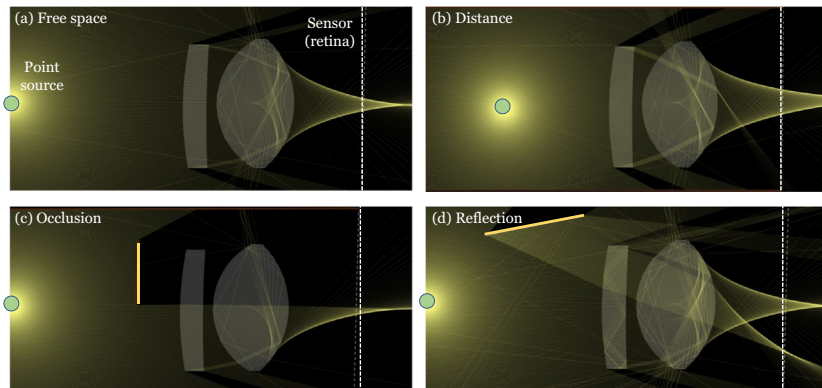
```
oi = oiCreate('diffraction limited');
oi = oiSet('oi','fnumber',5.6);
oiPlot(oi,'psf 550');
```

It is often useful to compute the diffraction limited retinal image as a standard to compare with real system performance. The diffraction-limited system is part of the general toolkit associated with “ideal observer” calculations that are widely used in vision science (Cottaris et al., 2020; Geisler, 1984).

## 3.2 Image formation: 3D

As noted above, calculating the retinal image of three-dimensional scenes requires accounting for phenomena that are not present in two-dimensional scenes (Fig. 7). First, the PSF depends on the distance to the object (depth of field), not just field height and wavelength. Second, rays from a point can be occluded by objects between that point and the eye (occlusion). Occlusion changes the PSF because it blocks a subset of the rays from points near the occluding edge. Third, rays from a point can reflect off multiple objects in the scene before reaching the eye (inter-reflections), and this too changes the PSF.

It is important to recognize that the second and third phenomena depend on the scene contents and cannot be predicted from knowledge of the optics alone.

**FIG. 7**

Three is not two. Calculating the retinal irradiance of a three-dimensional scenes requires accounting for phenomena that do not arise in two-dimensional scenes. (a) As a baseline, the rays from a point (green dot) are traced through free space and simple optics, roughly like the cornea and lens, and form an image of the point at the retina (sensor plane). (b) Changing the distance to the point changes the width of the PSF at the retina. (c) A nearby occluding object prevents a subset of the rays from the point from reaching the retina, changing the centroid location and spread of the PSF (occlusion). (d) Rays scattered from other objects in the scene can change the PSF (inter-reflections). Occlusion and inter-reflections depend on the scene content. The point spread function also varies with field height and pupil (aperture) size (not illustrated).

These inherently 3D effects can be accounted for using physically based computer graphics software, such as PBRT (Pharr et al., 2016) and Mitsuba (Nimier-David et al., 2019). ISET3d uses the PBRT software, with some custom extensions, to calculate the retinal spectral irradiance imaged through complex optics models, including the human eye (Lian et al., 2019). Three-dimensional computer graphics calculations account for occlusion and the large effect of surface inter-reflections, in addition to the choice of the lighting spectral distribution. Such calculations are relevant for complex environments, and may be helpful for interior design applications.

Ray tracing calculations through a model eye capture many properties of visual encoding; but they do not capture the higher order aberrations in the eye's optics that can be measured with wavefront sensors, and they are computationally expensive. To model the retinal image expected for a specific person, with stimuli on a flat display, particularly over a small region of the retina, approximating with a shift-invariant PSF and obtaining the PSF using adaptive optics measurements is more precise. Hence, scientists and engineers may have interest in both types of calculations.

## 4 Light transduction

There are three major light-sensitive retinal cell types. Two of these, the rods and cones, were described by van Leeuwenhoek in 1722. A functional role for these cells was suggested by Trevarinus in 1834 (Anon., 1935), and our understanding of their structure, function, and chemistry is relatively advanced. The existence of a third type of light-sensitive retinal cell was inferred relatively recently from the observation that animals without rods and cones still had light-entrained circadian rhythms (Freedman et al., 1999; Provencio et al., 2000). Subsequently, the light-sensitive pigment mediating this effect (melanopsin), and then the ipRGCs, which contain the pigment in their membrane, were identified (Berson et al., 2002). A multiplicity of ipRGC cell types, with different structure and central projections, have been found in both rodent (Lazzerini Ospri et al., 2017) and human (Hannibal et al., 2017; Liao et al., 2016; Nasir-Ahmad et al., 2019). The ipRGC responses can be caused directly by photons absorbed by melanopsin in their cell membrane, as well as by signals initiated in the rods and cones.

### 4.1 Rod and cone photoreceptors

Our understanding of the rods and cones is sufficient to enable quantitative modeling of how they encode retinal irradiance. Fig. 8a illustrates the structure of the retina and the location of the rod and cone receptors within it. Fig. 8b provides a schematic of the receptors themselves, and illustrates how light-sensitive pigment (photopigment) is situated within them. Light enters the inner segment of a receptor after passing through the retina. The inner segment acts as a waveguide, concentrating the light incident at the inner segment into the outer segment. The outer segment is dense with photopigment. As light enters the outer segment there is a wavelength-dependent probability that a discrete packet of energy (photon) will be absorbed by the pigment. The chance that a photon absorption isomerizes<sup>f</sup> the photopigment molecule is about two-thirds (Rodieck, 1998). In ISETBio, we refer to isomerizations as excitations for simplicity. We describe the calculation of cone excitations from the retinal irradiance in 4.1.1 below.

Light-sensitive molecules are present in the earliest life forms (Deisseroth, 2021), and the molecular form of these molecules has been largely conserved in the photopigments present in the human retina (Jacobs, 2009; Sharpe et al., 1999). Each class of cones contains a distinct type of opsin (photopigment): these classes are the long-wavelength-sensitive (L) cones, the middle-wavelength-sensitive (M) cones, and the short-wavelength-sensitive (S) cones. The corresponding photopigments are referred to as the L, M, and S photopigments.<sup>g</sup> The spectral absorptance differs between the

<sup>f</sup>Changes the molecule to another isomer.

<sup>g</sup>These are also called erythrolabe, chlorolabe, and cyanolabe, respectively.

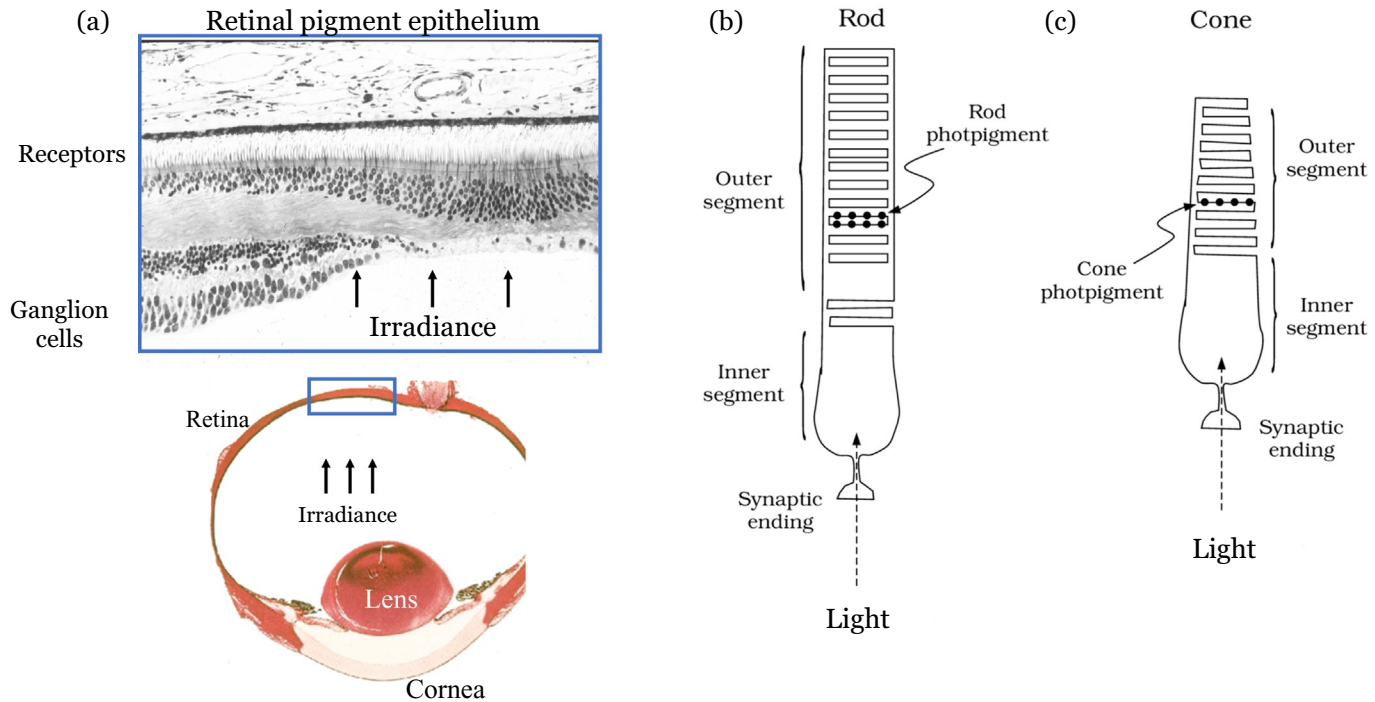


**FIG. 8**

Photoreceptors in context. The photoreceptors play an essential role in visual encoding. (a) Light from the scene incident at the cornea is transformed into an image at the retina. The retinal irradiance passes through the cells in the retina, arriving at the receptor layer. (b, c) The rods and cones have an entrance aperture near the synaptic ending. The inner segment acts as a waveguide, bringing the light through the outer segment, which contains the light sensitive photopigment.

*Images from Wandell, B. A., 1995. Foundations of Vision. Sinauer, Sunderland, MA.; Fig 3.2.*

three pigments (Fig. 10b), and the spectral absorptance differences can be traced to specific sequences in the photopigments' genetic codes (Nathans, 1999; Neitz and Neitz, 2011).

The rods, a second major class of retinal light-sensitive cells, encode retinal irradiance in much the same way as the cones. The initial encoding is the excitation of the rod photopigment, rhodopsin. Rhodopsin is used for light encoding in many species (Wald, 1974); we hasten to add that rhodopsin is also present and conserved in species that live in niches with virtually no light (Crandall and Hillis, 1997). This raises the possibility that rhodopsin is used for functions apart from vision.

The principles for computing rod excitations follow those for cone excitations, but the detailed parameters differ. There are several important differences from the point of view of vision, however. First, there is just one class of rods. Second, the rods have higher sensitivity than the cones, responding effectively to the absorption of a single photon. This enables the rod system to provide useful visual information at very low light levels. The higher sensitivity comes at a cost—the rods saturate at much lower light-levels than the cones. Thus, they provide little useful visual information under typical daylight conditions. Conversely, the cones do not support vision at low light levels. Third, there are no rods in the central fovea. Fourth, although the rod apertures are quite small, the outputs of multiple (say, 20) rods are combined at an early stage in the retina. Thus, the rod circuitry has a relatively large input referred aperture. Fifth, the rod temporal dynamics are much slower than the cone dynamics. In summary, rod-mediated vision is monochromatic, operates at low light levels, is absent in central vision, does not support high spatial resolution, and is sluggish.

ISETBio does not currently implement calculation of excitations for the rods. Some work would need to be done to simulate the positions of the rods, which appear in the interstices between the cones at visual field eccentricities outside the fovea. Rods also waveguide light differently from cones, so a different approximation to their entrance aperture would need to be implemented.

#### **4.1.1 Calculating excitations**

For computational reasoning we often calculate the spatial pattern of excitations in the photoreceptor mosaic. This requires knowledge of the scene spectral radiance,  $E(\lambda)$ , lens spectral transmission,  $l(\lambda, D_l)$ , the macular pigment transmission,  $m(\lambda, D_m)$ , and the photopigment spectral absorptance  $p(\lambda, D_p)$ . The lens, macular pigment, and photopigment absorbance spectra are tabulated in standards, and methods for calculating with these quantities are included in ISETBio.

There are simple principles used to calculate absorption and transmittance. We describe these principles using the computation of photopigment absorption as an example; the same principles may be used to compute lens and macular pigment transmission, which is one minus the probability of absorption.

For a sufficiently thin layer of pigment, the probability of absorption is proportional to the thickness ( $\delta$ ):

$$p(\lambda, \delta) = a_p(\lambda)\delta \quad (4)$$

Suppose we consider the pigment as comprising  $N$  thin layers ( $D_p = N\delta$ ). The probability of absorption is one minus the probability of not being absorbed in  $N$  thin layers<sup>b</sup>:

$$\begin{aligned} p(\lambda, D) &= 1 - (1 - p(\lambda, \delta))^N \\ &= 1 - (1 - a_p(\lambda)\delta)^N \\ &= 1 - \left(1 - \frac{a_p(\lambda)D_p}{N}\right)^N. \end{aligned} \quad (5)$$

In the limit as the layer thickness  $\delta$  becomes small,  $N$  becomes large and the probability of absorption is:

$$\begin{aligned} p(\lambda, D_p) &= \lim_{N \rightarrow \infty} 1 - \left(1 - \frac{a_p(\lambda)D_p}{N}\right)^N \\ &= 1 - e^{-a_p(\lambda)D_p} \end{aligned} \quad (6)$$

We refer to  $a_p(\lambda)$  as the absorptance spectrum of the pigment, and  $D_p$  as the pigment density. Often  $a_p(\lambda)$  is normalized to a peak of one, and  $D_p$  is expressed with respect to this convention. Because  $a_p(\lambda)$  and  $D_p$  appear only through their product in Eq. (6), other conventions would work equally well.

Variation in the densities of the lens, macular, and photopigments ( $D_l$ ,  $D_m$ ,  $D_p$ ) arises between people, over time, and across the surface of the retina (Asano et al., 2016; Stockman, 2019; Webster and MacLeod, 1988). The absorbance functions  $a_l(\lambda)$  and  $a_m(\lambda)$  of the lens and macular pigment are thought to be relatively consistent across people, although the lens absorbance does change somewhat in spectral shape with age. There are significant variations, however, in the photopigment absorbance spectra  $a_p(\lambda)$ . These variations can be specified in the ISETBio calculations.

#### 4.1.2 Principle of Univarience

The amount of energy,  $E$ , in a photon depends on its wavelength (Planck's relationship).

$$E = \frac{hc}{\lambda} = \frac{1.986 \times 10^{-16} \text{ J nm photon}^{-1}}{\lambda} \quad (7)$$

where  $h$  is Planck's constant and  $c$  is the speed of light. In principle, the size of the photocurrent initiated by an absorption might depend on the wavelength-dependent energy; but, this is not the case. Rather, the receptor output depends upon the number of photopigment excitations without regard to the energy in the specific photons that caused those excitations. This is called the Principle of Univarience (Rushton, 1972). For this reason most ISETBio calculations are grounded in units of photons.

We do note that for calculating spectral transmission the choice of units makes no difference: the fraction transmitted is the same whether using energy or photons.

---

<sup>b</sup>The probability of transmission is one minus the probability of absorption,  $1 - p(\lambda, D_p)$ , and vice versa. In this, we neglect back scatter.

The units are critical, however, for certain important CIE standards, such as luminance, illuminance, and the XYZ functions. These are defined in terms in units of energy, and the need to account for units is an essential part of the software. The ISETBio functions that simplify conversion between energy (Joules, Watts) and photons (quanta, quanta/sec) are

```
photons = Energy2Quanta(wavelength, energy);
energy = Quanta2Energy(wavelength, photons);
```

#### 4.1.3 Cone fundamentals

Under daylight or bright moonlight conditions, the brain uses cone excitations to understand the visual environment. Accounting for the optics is one important aspect of calculating the cone excitations. In addition, we need to know a few additional facts. First, we must establish the light absorbing properties and density of the cone photopigment. Second, we must know the diameter of entrance aperture (generally taken to be the diameter of the inner segment/outer segment junction as indicated in Fig. 8). Third, we must estimate the spectral transmissions of the retinal components the light passes through en-route to the photopigment. And fourth, we must specify how the spatial packing of the cones varies across the retina. We treat each of these, in turn.

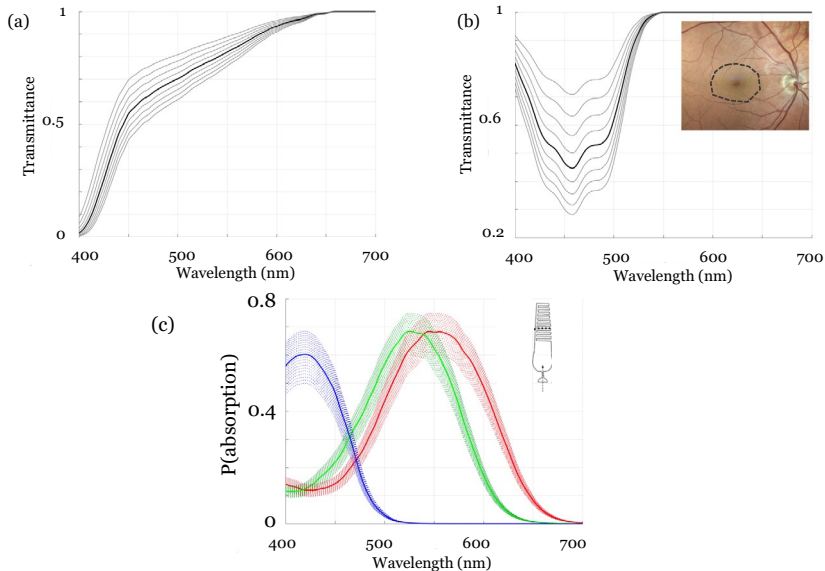
We calculate the number of excitations ( $N_e$ ) for a photoreceptor using Eq. (8). The equation combines spectral transmission of the lens  $l(\lambda, D_l)$  and macular pigment  $m(\lambda, D_m)$ , and the absorption of the photopigment  $p(\lambda, D_p)$ . The range of transmittance and absorption curves for plausible ranges of the densities are illustrated in Fig. 9.

$$F(\lambda; D) = l(\lambda, D_l)m(\lambda, D_m)p(\lambda, D_p) \quad (8)$$

$$N_e = \int_{\lambda} E(\lambda)F(\lambda; D)d\lambda$$

To use ISETBio to calculate a range of lens transmission curves we use this code (Fig. 10):

```
ieNewGraphWin;
thisLens = Lens;
for dd = 0.8:0.1:1.2
    thisLens.density = dd;
    plot(thisLens.wave,thisLens.transmittance);
    hold on;
end
grid on; xlabel('Wavelength (nm)'); ylabel('Transmittance')
```

**FIG. 9**

Spectral properties of visual system components that determine the input-referred quantum efficiency of the cones. (a) The crystalline lens dramatically reduces the fraction of short wavelength light transmitted to the retina. The optical density of the lens varies between people and with age. (b) The macular pigment is present in foveal, but not peripheral, regions of the retina. The pigment density in the fovea varies across people and with disease. (c) The optical density of the cone photopigment varies between people and across the retina. In all panels the *dark solid curve* is the standard and *lighter curves* are variations.

An excitation (isomerization) initiates a sequence of reactions within the outer segment: the *phototransduction cascade*. The consequence of these reactions is to open ion channels in the outer segment membrane, causing a net inward flow of ionic current. This photocurrent leads to a voltage change in the cone inner segment, modulating the neurotransmitter release at the synapse. ISETBio implements a model of this dynamic process for the cones, including a light-level dependency that modifies the gain and dynamics of the photoreceptor current. The model relies on measurements described in the literature (Angueyra-Aristizábal, 2014; Pugh and Lamb, 1993, 2000). ISETBio includes code to estimate the photoreceptor current, but we do not describe these methods here.

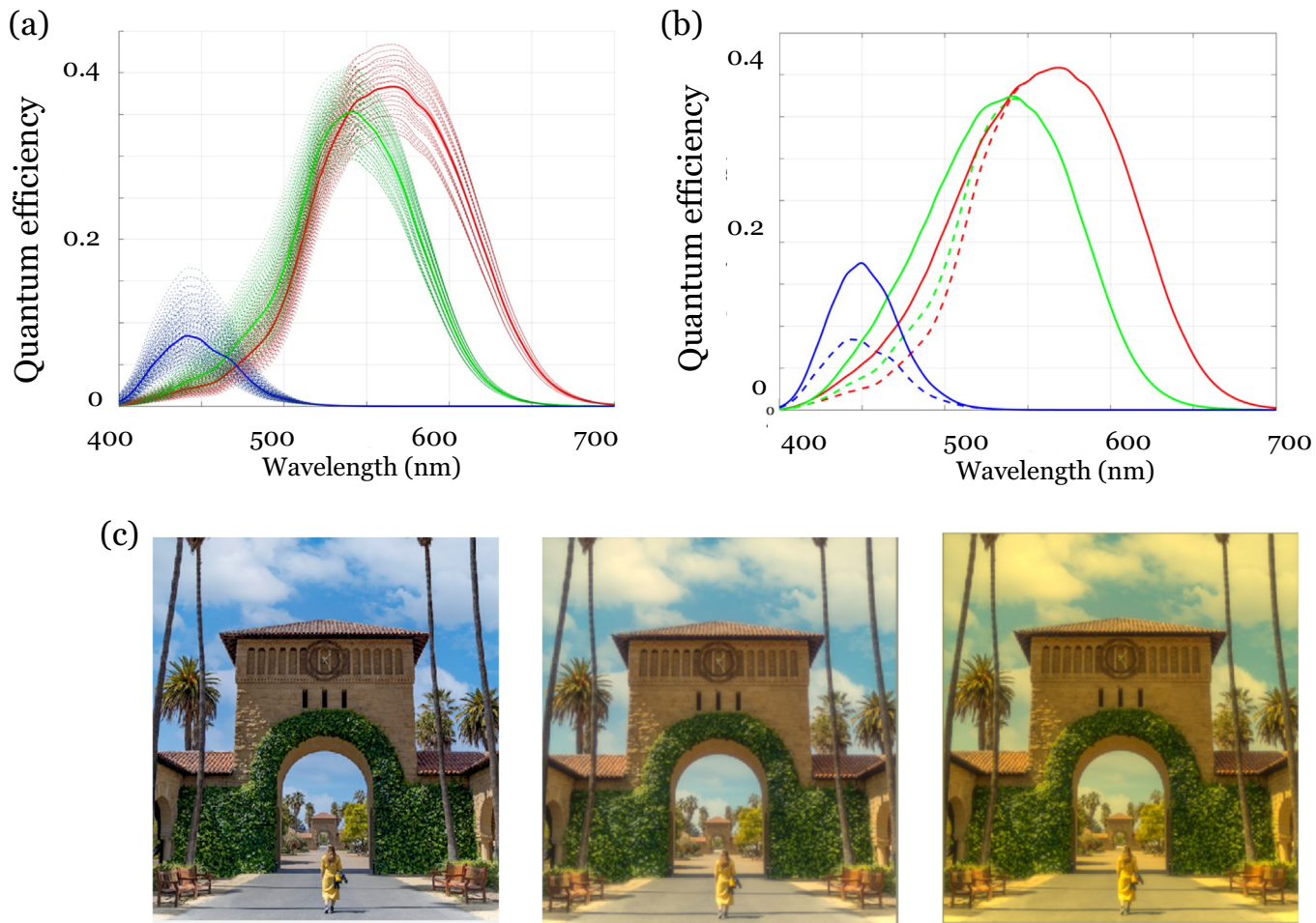


**FIG. 10**

Cone fundamentals. The cone excitation calculations start with the stimulus (scene spectral radiance). The transmission through the lens and macular pigment combined with the cone absorptance form a spectral function called the *cone fundamental*. The fundamental is the input-referred spectral quantum efficiency of the cone. (a) The fundamental is defined using standard values (*solid curves*) for the lens, macular pigment and photopigment. There are significant variations (*dotted curves*) across the population, with the largest variation in the spectrum below 550 nm. (b) There is a reliable difference between the cone fundamentals near the fovea (*dashed lines*) and periphery because of the macular pigment (*solid lines*). (c) The three images give an impression of how the scene spectral radiance (*left*) is transformed as it passes through the lens (*middle*) and macular pigment (*right*). The ISETBio implementation includes lens factors as part of the retinal spectral irradiance (*oi*) computation; it includes macular pigment factors as part of the cone mosaic (*cMosaic*) computations.

#### 4.1.4 Cone mosaic

The spatial arrangement of the photoreceptors is an important factor limiting visual encoding. The properties of the cone spatial mosaic have been measured over the last thirty years. The important work of Curcio and her collaborations (Curcio et al., 1990) set the stage, and more has been learned from the new adaptive optics methods that measure both the spatial arrangement and cone types in the living human eye (Hofer and Williams, 2014). These data provide an excellent foundation that enables us generate synthetic cone mosaics that match the statistical properties of observed mosaics.

[Fig. 11](#) is a simulated cone mosaic for a horizontal strip starting at the fovea and extending 6 degrees (2 mm) eccentrically. The code to create this mosaic and plot the images using ISETBio is simple.

```
cmP = cMosaicParams;           % Return the settable parameters
cmP.positionDegs = [3,0];       % Center position of the mosaic
cmP.sizeDegs = [6 1];          % Size of the mosaic
cm = cMosaic(cmP);            % Create the cone mosaic
cm.visualize                  % Visualize the mosaic
```

The figure illustrates several properties that are important for visual encoding. First, the cone density is highest in the center of the retina (the fovea), decreasing significantly with eccentricity even over this relatively narrow range. Second, the sampling densities of the three classes of cones differ. In the typical eye the L cones are the highest proportion (60%), the M cones comprise about 30% and the S-cones make up about 10%. These proportions are typical, but we hasten to add that the L/M ratios differ substantially between people so that the typical number is not necessarily a good estimate for any individual (Hofer and Williams, 2014). The cone density at the fovea also differs significantly between individuals (Curcio et al., 1990).

Within the mosaic, the L- and M-cone positions are nearly randomly placed. The S-cones, however, appear to form a more regular sampling grid, at least in some subjects (Hofer et al., 2005). In a small region in the very center (about 20 min of visual field diameter) of the fovea, there are no S-cones. The peak S-cone density is at 1 degree of visual field eccentricity.

The cone apertures and photopigment optical densities vary with eccentricity. This variation, incorporated in the ISETBio computation, significantly impacts the number of excitations in a single cone: The increase in the cone inner segment aperture accounts for about a nine-fold increase in excitations. This increase opposes the effect of the decreased sampling density. The ISETBio calculation from a scene to the mosaic of cone excitations, accounting for all of the factors, is

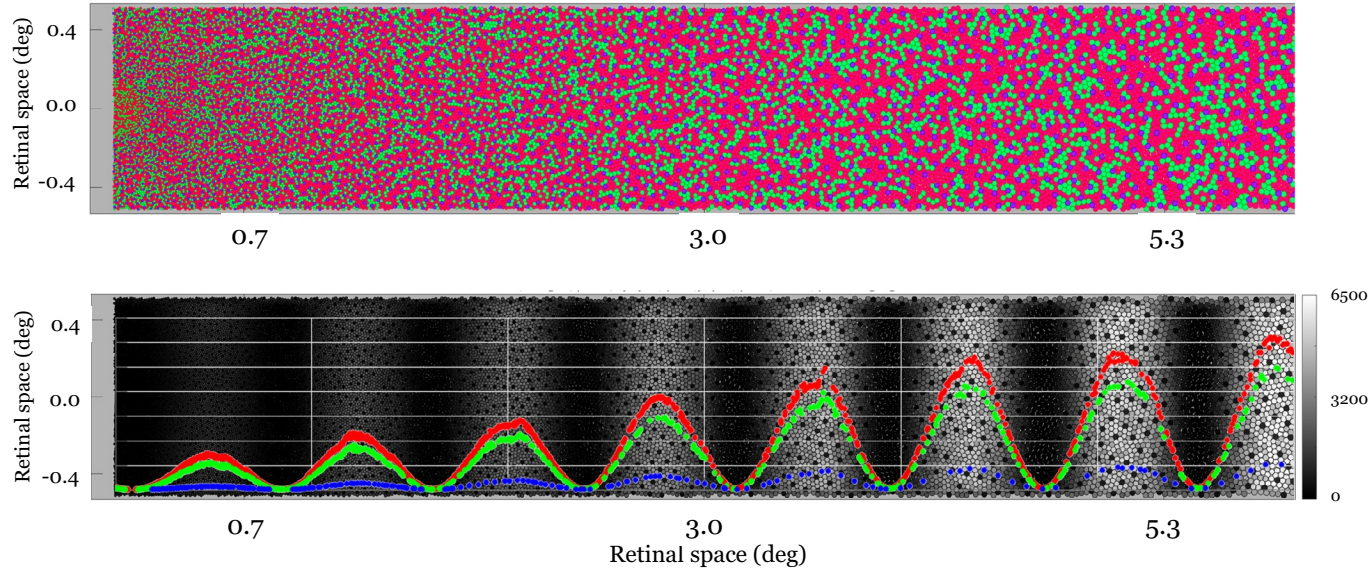


**FIG. 11**

Cone sampling and aperture size. (*Top*) The spatial sampling density of the cone photoreceptors changes substantially across the retina, decreasing from the fovea (*left*) to periphery (*right*). The image shows a narrow strip along the horizontal axis. As sampling density decreases, aperture size increases. Consequently for a constant irradiance pattern the number of excitations per cone increases. (*Bottom*) The *gray scale* image shows the estimated number excitations in the cone mosaic in response to a harmonic stimulus of constant contrast across the image. The *colored curves* show the mean number of excitations for each of the three cone types (scale bar at the *right*).

```
% The scene spectral radiance
scene = sceneCreate('dead leaves');
scene = sceneSet(scene,'fov',2);

% The optical image (retinal spectral irradiance)
oi = oiCreate;
oi = oiCompute(oi,scene);

% The cMosaic
cmP = cMosaicParams; cmP.positionDegs = [0,0]; cmP.sizeDegs = [2 2];
cm = cMosaic(cmP);
allE = cm.compute(oi);

% Show an image of the excitations
cm.plot('excitations',allE); colormap("jet")
```

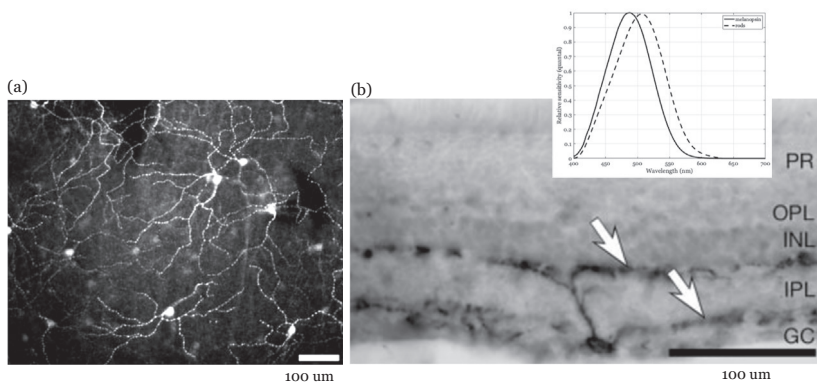
The mean cone excitation rate is calculated in excitations per second, and the number of excitations is Poisson distributed. Thus knowing the mean excitations tells us the signal-to-noise ratio of the information carried by each cone. This information is critical for predicting the precision of visual judgments supported by the transduced information from any visual stimulus (Cottaris et al., 2020).

ISETBio accounts for many photoreceptor mosaic properties, but there is one important exception. We do not yet simulate the rods interlaced within the cone mosaic.

## 4.2 Intrinsically photosensitive retinal ganglion cells

The third major class of retinal light-sensitive cells are a significant departure from the photoreceptors. First, their cell bodies are in the ganglion cell layer of the retina. Second, they contain light-sensitive melanopsin in their cell bodies and dendritic arbors (Fig. 12). These intrinsically photosensitive retinal ganglion cells (ipRGCs) are subtyped based upon their morphology, retinal circuitry, light responses, and central projections. In animal models the projection destinations suggest that ipRGC signals from certain subtypes impact circadian rhythms, have acute effects on sleep, and play a role in the pupillary light reflex (Lazzerini Osibri et al., 2017). Multiple subtypes of ipRGCs have also been identified in human, again based on the size and spatial distribution of their dendritic arbors (Hannibal et al., 2017; Liao et al., 2016; Nasir-Ahmad et al., 2019).

In addition to their intrinsic light sensitivity, ipRGCs are driven by input from the rods and cones. The photoreceptor signals are communicated through intermediate bipolar cells and via lateral connections to horizontal and amacrine cells. The ipRGC circuitry differs significantly from the circuitry of other ganglion cells; for example, they can receive ON-bipolar inputs, but surprisingly these arise in the OFF-sublamina of the inner plexiform layer. In this sense, the ipRGCs differ from other retinal ganglion cells.

**FIG. 12**

Spatial distribution of melanopsin in the ipRGCs. (a) An inplane retinal image stained for melanopsin. The *large bright spots* are retinal ganglion cell bodies, and the *thin bright lines* are melanopsin in dendrites. (b) A retinal cross section stained for melanopsin. The cell body is in the retinal ganglion cell layer. The dendrites are localized in two different layers. The graphical inset shows the relative spectral quantal efficiency of melanopsin (*solid*) and rods (*dashed*).

*Images from Provencio, I., Rodriguez, I. R., Jiang, G., Hayes, W. P., Moreira, E. F., Rollag, M. D., 2000.*

*A novel human opsin in the inner retina. J. Neurosci. 20 (2), 600–605.*

For multiple reasons, melanopsin excitation calculations differ from the photoreceptor excitation calculations. First, in cones and rods, photoreceptor pigment is localized to the outer segment, spanning a diameter of only a few microns, and the identity of the photoreceptor thus contains high-resolution information about the retinal location of the exciting photons. In contrast, melanopsin in a single ipRGC spans the cell body and dendritic arbor, between 250 and 1000 microns of diameter (Nasir-Ahmad et al., 2019) (Fig. 12a). Second, a generalized Principle of Univariate does not apply to the ipRGCs. Univariate ordinarily refers to the fact that the wavelength of a photon excitation does not change the response. The generalized principle is that an excitation anywhere—cell body versus dendritic arbor—would produce the same response. This is unlikely to be true, and this may be significant because the density of cell bodies and distribution of dendritic arbors differ between the various classes of ipRGCs. Third, the melanopsin photochemistry differs from the photoreceptor transduction cascade (Brown et al., 2013; Do and Yau, 2010; Enezi et al., 2011). Finally, for the ipRGCs more generally, signals initiated in the photoreceptors combine with the melanopsin initiated intrinsic signals, limiting our ability to make predictions of the ipRGC responses.

With these limitations, we can estimate only the relative impact of the spectral irradiance on the ipRGC melanopsin responses. We treat the melanopsin pigment as a thin layer, defined by a spectral absorbance (see Eq. 4). Given this, we can

calculate the efficacy of a spectral irradiance by multiplying it by the CIE standard melanopsin fundamental (CIE2018, 2022). The fundamental is input-referred, just like the cone fundamentals. The melanopsin fundamental is similar to the rod fundamental (Fig. 12, inset). It depends significantly on the lens transmission. The macular pigment is located in the Henle fiber layer in the fovea and in the inner nuclear layer (below the cell bodies) in the parafovea. Thus, the macular pigment is not on the light path to the melanopsin in the ipRGCs (Trieschmann et al., 2008).

Understanding the impact of ipRGC cells on vision is enhanced even by these approximate calculations. As examples, we can estimate (1) the spatial resolution of the melanopsin-mediated ipRGC mosaics from the cell body spacing with eccentricity (Liao et al., 2016), and (2) the relative impact of a spectral irradiance on melanopsin excitations (Spitschan et al., 2014, 2017). As we learn more, perhaps enabling us to estimate the effective number of excitations—and thus the Poisson variability—we can extend our understanding of the visual representation supported by the ipRGCs.

---

## 5 Example calculations

Many components of the figures in this chapter were created using the ISETBio software. The scripts we used are stored in an online repository. To view the code please visit the repository wiki page.<sup>i</sup> To run the code you must have Matlab installed and the ISETBio software<sup>j</sup> on your Matlab path.

---

## 6 Summary

Three centuries of research have provided significant information about the light around us and the way the human eye encodes that light. Recent advances in technology and software make it possible to model a relatively complex light environment and the visual encoding using readily available computers. This chapter describes principles of the visual encoding along with software that enables scientists and engineers to simulate the early visual encoding.

---

<sup>i</sup><https://github.com/isetbio/isetbioencoding/wiki>.

<sup>j</sup><https://github.com/isetbio/isetbio>.

## References

- Angueyra-Aristizábal, J.M., 2014. The Limits Imposed in Primate Vision by Transduction in Cone Photoreceptors. University of Washington Libraries.
- Anon., 1935. Historical review. *Acta Ophthalmol.* 13 (S6), 13–28.
- Asano, Y., Fairchild, M.D., Blondé, L., 2016. Individual colorimetric observer model. *PLoS One* 11 (2), e0145671.
- Bedggood, P., Daaboul, M., Ashman, R., Smith, G., Metha, A., 2008. Characteristics of the human isoplanatic patch and implications for adaptive optics retinal imaging. *J. Biomed. Opt.* 13 (2), 024008.
- Berson, D.M., Dunn, F.A., Takao, M., 2002. Phototransduction by retinal ganglion cells that set the circadian clock. *Science* 295 (5557), 1070–1073.
- Brainard, D.H., Stockman, A., 2010. Colorimetry. In: Bass, M., DeCusatis, C., Enoch, J., Lakshminarayanan, V., Li, G., Macdonald, C., et al. (Eds.), *The Optical Society of America Handbook of Optics*, Third ed., Volume III: Vision and Vision Optics. McGraw Hill, New York. 10.1–10.56.
- Brainard, D.H., Pelli, D.G., Robson, T., 2002. Display characterization. *Signal Process.* 80, 2–067.
- Brown, T.M., Allen, A.E., al Enezi, J., Wynne, J., Schlangen, L., Hommes, V., Lucas, R.J., 2013. The melanopic sensitivity function accounts for Melanopsin-Driven responses in mice under diverse lighting conditions. *PLoS One* 8 (1), e53583.
- CIE2018, 2022. CIE system for metrology of optical radiation for ipRGC-Influenced responses to light. (accessed: 11.02.22) <https://cie.co.at/publications/cie-system-metrology-optical-radiation-iprgc-influenced-responses-light-0>.
- Cottaris, N.P., Wandell, B.A., Rieke, F., Brainard, D.H., 2020. A computational observer model of spatial contrast sensitivity: effects of photocurrent encoding, fixational eye movements, and inference engine. *J. Vis.* 20 (7), 17.
- Crandall, K.A., Hillis, D.M., 1997. Rhodopsin evolution in the dark. *Nature* 387 (6634), 667–668.
- Curcio, C.A., Sloan, K.R., Kalina, R.E., Hendrickson, A.E., 1990. Human photoreceptor topography. *J. Comp. Neurol.* 292 (4), 497–523.
- Deisseroth, K., 2021. From microbial membrane proteins to the mysteries of emotion. *Cell* 184 (21), 5279–5285.
- Do, M.T.H., Yau, K.-W., 2010. Intrinsically photosensitive retinal ganglion cells. *Physiol. Rev.* 90 (4), 1547–1581.
- Enezi, J.A., Revell, V., Brown, T., Wynne, J., Schlangen, L., Lucas, R., 2011. A “melanopic” spectral efficiency function predicts the sensitivity of melanopsin photoreceptors to polychromatic lights. *J. Biol. Rhythms* 26 (4), 314–323.
- Fleming, R.W., 2017. Material perception. *Annu. Rev. Vis. Sci.* 3, 365–388.
- Freedman, M.S., Lucas, R.J., Soni, B., von Schantz, M., Muñoz, M., David-Gray, Z., Foster, R., 1999. Regulation of mammalian circadian behavior by non-rod, non-cone, ocular photoreceptors. *Science* 284 (5413), 502–504.
- Geisler, W.S., 1984. Physical limits of acuity and hyperacuity. *J. Opt. Soc. Am. A* 1 (7), 775–782.
- Goossens, T., Lyu, Z., Ko, J., Wan, G., Farrell, J., Wandell, B., 2022. Ray-transfer functions for camera simulation of 3D scenes with hidden lens design. *arXiv*. 2202.08880.
- Hannibal, J., Christiansen, A.T., Heegaard, S., Fahrenkrug, J., Kiilgaard, J.F., 2017. Melanopsin expressing human retinal ganglion cells: Subtypes, distribution, and intraretinal connectivity. *J. Comp. Neurol.* 525 (8), 1934–1961.

- Heasly, B.S., Cottaris, N.P., Lichtman, D.P., Xiao, B., Brainard, D.H., 2014. RenderToolbox3: MATLAB tools that facilitate physically based stimulus rendering for vision research. *J. Vis.* 14 (2), 6. 6.
- Hofer, H.J., Williams, D.R., 2014. Color vision and the retinal mosaic. In: Chalupa, L.M., Werner, J.S. (Eds.), *The New Visual Neurosciences*. MIT Press, Cambridge, MA, pp. 469–483.
- Hofer, H., Carroll, J., Neitz, J., Neitz, M., Williams, D.R., 2005. Organization of the human trichromatic cone mosaic. *J. Neurosci.* 25 (42), 9669–9679.
- IEC, 1999. IEC 61966-2-1:1999: default RGB colour space—sRGB. (accessed: 24.12.21) <https://webstore.iec.ch/publication/6169>.
- Jacobs, G.H., 2009. Evolution of colour vision in mammals. *Philos. Trans. R. Soc. Lond. B Biol. Sci.* 364 (1531), 2957–2967.
- Jaeken, B., Artal, P., 2012. Optical quality of emmetropic and myopic eyes in the periphery measured with high-angular resolution. *Invest. Ophthalmol. Vis. Sci.* 53 (7), 3405–3413.
- Lazzerini Osprí, L., Prusky, G., Hattar, S., 2017. Mood, the circadian system, and melanopsin retinal ganglion cells. *Annu. Rev. Neurosci.* 40, 539–556.
- Lian, T., MacKenzie, K.J., Brainard, D.H., Cottaris, N.P., Wandell, B.A., 2019. Ray tracing 3D spectral scenes through human optics models. *J. Vis.* 19 (12), 23.
- Liang, J., Williams, D.R., Miller, D.T., 1997. Supernormal vision and high-resolution retinal imaging through adaptive optics. *J. Opt. Soc. Am. A Opt. Image Sci. Vis.* 14 (11), 2884–2892.
- Liao, H.-W., Ren, X., Peterson, B.B., Marshak, D.W., Yau, K.-W., Gamlin, P.D., Dacey, D.M., 2016. Melanopsin-expressing ganglion cells on macaque and human retinas form two morphologically distinct populations. *J. Comp. Neurol.* 524 (14), 2845–2872.
- Lyu, Z., Kripakaran, K., Furth, M., Tang, E., Wandell, B., Farrell, J., 2021. Validation of image systems simulation technology using a Cornell box. arXiv. 2105.04106.
- Maxwell, J.C., 1860. On the theory of compound colours and the relations of the colours of the spectrum. *Phil. Trans. R. Soc. Lond.* 150, 57–84.
- Nasir-Ahmad, S., Lee, S.C.S., Martin, P.R., Grünert, U., 2019. Melanopsin-expressing ganglion cells in human retina: morphology, distribution, and synaptic connections. *J. Comp. Neurol.* 527 (1), 312–327.
- Nathans, J., 1999. The evolution and physiology of human color vision: insights from molecular genetic studies of visual pigments. *Neuron* 24 (2), 299–312.
- Neitz, J., Neitz, M., 2011. The genetics of normal and defective color vision. *Vision Res.* 51 (7), 633–651.
- Nimier-David, M., Vicini, D., Zeltner, T., Jakob, W., 2019. Mitsuba 2: a retargetable forward and inverse renderer. *ACM Trans. Graph.* 38 (6), 1–17.
- Pharr, M., Jakob, W., Humphreys, G., 2016. *Physically Based Rendering: From Theory to Implementation*. Morgan Kaufmann (September).
- Polans, J., Jaeken, B., McNabb, R.P., Artal, P., Izatt, J.A., 2015. Wide-field optical model of the human eye with asymmetrically tilted and decentered lens that reproduces measured ocular aberrations. *Optica* 2 (2), 124–134.
- Pont, S.C., 2019. Light: toward a transdisciplinary science of appearance and atmosphere. *Annu. Rev. vis. Sci.* 5, 503–527.
- Provencio, I., Rodriguez, I.R., Jiang, G., Hayes, W.P., Moreira, E.F., Rollag, M.D., 2000. A novel human opsin in the inner retina. *J. Neurosci.* 20 (2), 600–605.
- Pugh Jr, E.N., Lamb, T.D., 1993. Amplification and kinetics of the activation steps in phototransduction. *Biochim. Biophys. Acta* 1141 (2-3), 111–149.

- Pugh, E.N., Lamb, T.D., 2000. Chapter 5 phototransduction in vertebrate rods and cones: molecular mechanisms of amplification, recovery and light adaptation. In: Stavenga, D.G., DeGrip, W.J., Pugh, E.N. (Eds.), *Handbook of Biological Physics*. vol. 3. North-Holland, pp. 183–255 (January).
- Rodieck, R.W., 1998. *The First Steps in Seeing*. Sinauer (August).
- Rushton, W.A.H., 1972. Pigments and signals in colour vision. *J. Physiol.* 220 (3). 1P–31P.
- Sharpe, L.T., Stockman, A., Jägle, H., Nathans, J., 1999. Opsin genes, cone photopigments, color vision, and color blindness. In: Sharpe, L.T., Gegenfurtner, K.R. (Eds.), *Color vision: From Genes to Perception*. Cambridge University Press, Cambridge, pp. 3–51.
- Spitschan, M., Jain, S., Brainard, D.H., Aguirre, G.K., 2014. Opponent melanopsin and S-cone signals in the human pupillary light response. *Proc. Natl. Acad. Sci. U. S. A.* 111 (43), 15568–15572.
- Spitschan, M., Bock, A.S., Ryan, J., Frazzetta, G., Brainard, D.H., Aguirre, G.K., 2017. The human visual cortex response to melanopsin-directed stimulation is accompanied by a distinct perceptual experience. *Proc. Natl. Acad. Sci. U. S. A.* 114 (46), 12291–12296.
- Stockman, A., 2019. Cone fundamentals and CIE standards. *Curr. Opin. Behav. Sci.* 30, 87–93.
- Thibos, L.N., Bradley, A., Still, D.L., Zhang, X., Howarth, P.A., 1990. Theory and measurement of ocular chromatic aberration. *Vision Res.* 30 (1), 33–49.
- Trieschmann, M., van Kuijk, F.J.G.M., Alexander, R., Hermans, P., Luthert, P., Bird, A.C., Pauleikhoff, D., 2008. Macular pigment in the human retina: histological evaluation of localization and distribution. *Eye* 22 (1), 132–137.
- Wald, G., 1974. Visual pigments and photoreceptors—review and outlook. *Exp. Eye Res.* 18 (3), 333–343.
- Wandell, B.A., 1995. *Foundations of Vision*. Sinauer, Sunderland, MA.
- Wandell, B., 2022. ISETCam wiki. (accessed: 06.03.22) <https://github.com/ISET/isetcam>.
- Wandell, B., Brainard, D., 2022. Principles and consequences of the initial visual encoding. In: Gregory, A.F., Colonius, H., Dzhafarov, E.N. (Eds.), *New Handbook of Mathematical Psychology*. vol. 3. Cambridge University Press, Cambridge.
- Wandell, B., Brainard, D., Cottaris, N., 2022. ISETBio wiki. (accessed: 06.03.22) <https://github.com/isetbio/isetbio>.
- Webster, M.A., MacLeod, D.I.A., 1988. Factors underlying individual differences in the color matches of normal observers. *JOSA A* 5 (10), 1722–1735.
- Zandi, B., Stefani, O., Herzog, A., Schlangen, L.J.M., Trinh, Q.V., Khanh, T.Q., 2021. Optimising metameric spectra for integrative lighting to modulate the circadian system without affecting visual appearance. *Sci. Rep.* 11 (1), 23188.